ACADEMIA ROMÂNĂ

Revue Roumaine de Chimie

https://www.icf.ro/rrch/

Rev. Roum. Chim.,
2026, *71*(3–4), 169–178
DOI: 10.33224/rrch.2026.71.3-4.02

PREPARATION AND PROPERTIES OF $Ce_{0.8}Ca_xLa_{0.2-x}O_{2-\delta}$ ELECTROLYTE MATERIALS FOR IT-SOFCs

Yang ZHAO,[a] Jingchen SUN,[a] Shiqi WANG,[a,b] Chang DU,[a,b] Fengshan YU[a,b] and Jie YANG[a,b,*]

[a] School of Energy Materials and Chemical Engineering, Hefei University, Anhui Hefei 230601, P.R. China
[b] Carbon Neutrality and Carbon Peaking Materials and Resource Chemical Laboratory, Hefei University, Hefei, Anhui, 230601, China

Received June 16, 2025

$Ce_{0.8}Ca_xLa_{0.2-x}O_{2-\delta}$ (x = 0, 0.04, 0.08, 0.12, 0.16, 0.2) fluorite oxides were synthesized via the Pechini method for their prospective application as electrolytes in intermediate-temperature solid oxide fuel cells (IT-SOFCs). The synthesized materials were characterized and confirmed to form a solid solution with a cubic fluorite structure. This study notably achieved a reduction in the sintering temperature of the materials, concomitant with an enhancement in their electrochemical properties, particularly conductivity. Post-sintering at 1250 °C, the density of the samples surpassed 96% of the theoretical density. To evaluate the ionic conductivity, electrochemical impedance spectroscopy was applied across a temperature range from 400 °C to 800 °C. Among the compositions investigated, $Ce_{0.8}Ca_{0.16}La_{0.04}O_{2-\delta}$ exhibited the highest conductivity of 0.078 $S \cdot cm^{-1}$ at the upper limit of the examined temperature range. Furthermore, this material displayed a notably low activation energy of 0.82 eV, underscoring its promising potential for IT-SOFC applications.

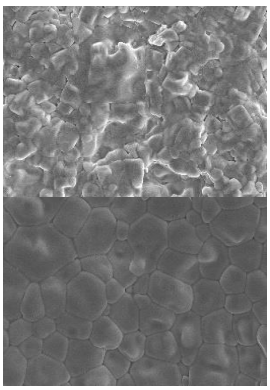

INTRODUCTION

Solid oxide fuel cells (SOFCs) have simple structure and energy conversion efficiency of high energy saving and the excellent property of little pollution.[1–4] For the present, petroleum, coal and other one-time energy have reached maximal height of mining.[3] And currently, there exists an energy shortage. Due to the extensive use of such one-time source energy, large amounts of toxic gases are made and the environment were heavily damaged.[5–9] Under such circumstances, the development and research of fuel cell has become an important direction for the development of new energy sources.[0–14]

Electrolyte, as an important component of fuel cells, has become a hot research topic. However, the key problem is its application limit in the low temperature sintering of ceramic performance and it is difficult to have adequate sintering strength or density. Previous scientific research has indicated that in the ceramic performance, certain metal ions doping can reduce the sintering temperature and enables it to have a good sintering activity.[15–18] Doped cerium oxide has good ionic conductivity at high temperatures which makes it a potential application as an electrolyte material in solid oxide fuel cells. The crystal structure of cerium oxide is a cubic fluorite structure, which is a surface-centered cubic (Fcc) lattice with a space group of Fm3m.

* Corresponding author: yangjhfuu@163.com

For CeO_2, the ionic radius of Ce^{4+} to that of O^{2-} is about 0.74 Å, and this ratio is suitable for forming a cubic fluorite structure. Due to its structural characteristics, the cubic fluorite structure can accommodate a higher concentration of oxygen vacancies, and have a good thermal stability.[19–21]

Pure CeO_2 showed low oxygen ion conductivity ($\sigma_{973\ K}$= 1.9×10^{-5} $S\cdot cm^{-1}$), and a high sintering temperature reached 1600 °C during preparation. The introduction of dopant can reduce the high sintering temperature of the material and improve the ionic conductivity of the material. Both the type and quantity of dopants play a critical role in the design of ceria-based electrolytes. Some studies proposed that doped ceria tends to exhibit higher electrical conductivity when the radius of dopant ions approaches the critical radius of 0.1093 nm.[22] According to Naeemakhtar Momin, the maximum conductivity of cerium oxide $Ce_{0.90}La_{0.1}O_{2-\delta}$(0.1 LDC) is 8.89×10^{-3} $S\cdot cm^{-1}$ at the sintering temperature of 1250 °C. The present experiments show that the introduction of La element can reduce the sintering temperature and still exhibit excellent ionic conductivity.[16] The introduction of the Ca element can reduce the sintering temperature of the CeO_2 system to 1400 °C with excellent electrochemical characteristics.[23] Consequently, in this experiment, with the application of CeO_2 as matrix, La^{3+}, Ca^{2+} were co-doped, to explore different proportion of $Ce_{0.8}Ca_xLa_{0.2-x}O_{2-\delta}$（x = 0, 0.04, 0.08, 0.12, 0.16, 0.2）electrolyte material performance of sintering activity, caused by the influence of density and dielectric properties. In previous studies of doubly doped cerium oxide systems, there has been significant success in reducing the sintering temperature of pure cerium oxide and improving the ion conductivity. For example, the optimal component ion conductivity of CeO_2 doping with Gd elements and Sm elements at 1500 °C can reach 3.1×10^{-2} $S\cdot cm^{-1}$.[24] $Ce_{0.8}Y_{0.2-x}Cu_xO_{2-\delta}$, the conductivity can reach 2.9×10^{-2} $S\cdot cm^{-1}$ at 1300 °C sintering.[25] Similarly, in the study of Kasarapu Venkataramana co-doped CeO_2, there is also an improvement in pure cerium oxide sintering temperature and conductivity. Ionic conductivity can reach 2.08×10^{-2} $S\cdot cm^{-1}$ by adopting La element and Dy element co-doping at 1300 °C.[26] The study shows that the sample density of La element and Ca element reaches 96% at 1250 °C, and the ionic conductivity reaches 7.8×10^{-2} $S\cdot cm^{-1}$, this is higher than the ionic conductivity of the previous cerium oxide double doped system.

MATERIALS AND METHODS

In this experiment, high-purity reagents $Ce(NO_3)_3\cdot6H_2O$ (99.99%, Aladdin), $Ca(NO_3)_2\cdot4H_2O$ (99.99%, Aladdin), and $La(NO_3)_3\cdot6H_2O$ (99.99%, Aladdin) were utilized, along with citric acid $C_6H_8O_7$ (99.99%, Sinopharm) and ethylene glycol $C_2H_6O_2$ (99.99%, Sinopharm), to prepare electrolyte materials with the stoichiometry $Ce_{0.8}Ca_xLa_{0.2-x}O_{2-\delta}$ (x = 0, 0.04, 0.08, 0.12, 0.16, 0.2). The Pechini method was employed for the preparation. Specifically, the nitrates were mixed with citric acid and ethylene glycol, stirred until a gel formed, and then allowed to fully gel. The resulting gel was ground into a powder, which was subsequently calcined at 700 °C for 2 hours. The calcined powder was milled, granulated, and tabletted to form discs with a diameter of 13 mm and a thickness of 1.5–2 mm under a pressure of 200 MPa. The ceramic elements were then sintered at 1250 °C. The flow chart of the sol gel preparation of $Ce_{0.8}Ca_xLa_{0.2-x}O_{2-\delta}$ is shown in Fig. 1.

The characterization methods employed in this study include the following techniques to comprehensively analyze the structure, morphology, thermal behavior, and electrochemical performance of the samples:

Fourier Transform Infrared Spectroscopy (FT-IR) was conducted using a Nicolet iS50 FT-IR spectrometer (Thermo Fisher Scientific, USA), with a test wavenumber range of 400~4000 cm^{-1} and a spectral resolution of 4 cm^{-1}. The sample was thoroughly ground with spectrally pure KBr at a mass ratio of 1:100 and then pressed into a transparent pellet *via* a hydraulic press for testing, aiming to eliminate background interference and identify the functional groups and chemical bond types in the sample.

Simultaneous Thermogravimetry-Differential Scanning Calorimetry (TG-DSC) was performed with an HCT-1 TG-DSC analyzer (China) under an air atmosphere to investigate the thermal behavior of the xerogel sample. The test temperature ranged from 35 to 800 ℃ at a heating rate of 10 ℃/min, accompanied by a nitrogen purge rate of 50 mL/min, which accurately recorded the mass changes and thermal effects during the thermal process and provided a basis for subsequent calcination and sintering procedures.

X-Ray Diffraction (XRD) measurements were carried out using a Rigaku Smart Lab SE X-ray diffractometer (Rigaku, Japan) equipped with a Cu

$K_{\alpha 1}$ radiation source (λ=1.5406 Å), operating at a tube voltage of 40 kV and a tube current of 40 mA. The scan range was set to 2θ=20°~80° with a step size of 0.02° and a scan rate of 5°/min, enabling phase identification, lattice parameter calculation, and crystallinity analysis of the samples.

Scanning Electron Microscopy (SEM) observations were performed with a 3200 scanning electron microscope (China) at an acceleration voltage of 10 kV and a working distance of 8 mm. Prior to testing, the sample was sputter-coated with gold to enhance conductivity, facilitating the observation of the sample surface morphology, cross-sectional structure, particle agglomeration state, and grain distribution.

Electrochemical Impedance Spectroscopy (EIS) and conductivity measurement were conducted using a CHI660E AC impedance analyzer (China), with a test frequency range of 0.1 Hz~1 MHz and a test temperature range of 400~800 ℃ at intervals of 50 ℃; each temperature point was held for 30 min to achieve thermal equilibrium. The sample was processed into a disk with a diameter of approximately 12 mm and a thickness of 0.1~0.15 mm, and silver paste was uniformly coated on both sides as electrodes, followed by annealing at 700 ℃ for 10 min in a muffle furnace to improve the contact stability between the electrodes and the sample. The four-probe method was utilized for testing, and the impedance data were fitted using ZSimpWin software. The total conductivity was calculated by the formula $\sigma_t = l/A \cdot R$ (where l denotes the sample thickness, A is the effective electrode area, and R_t represents the total resistance).[27,28]

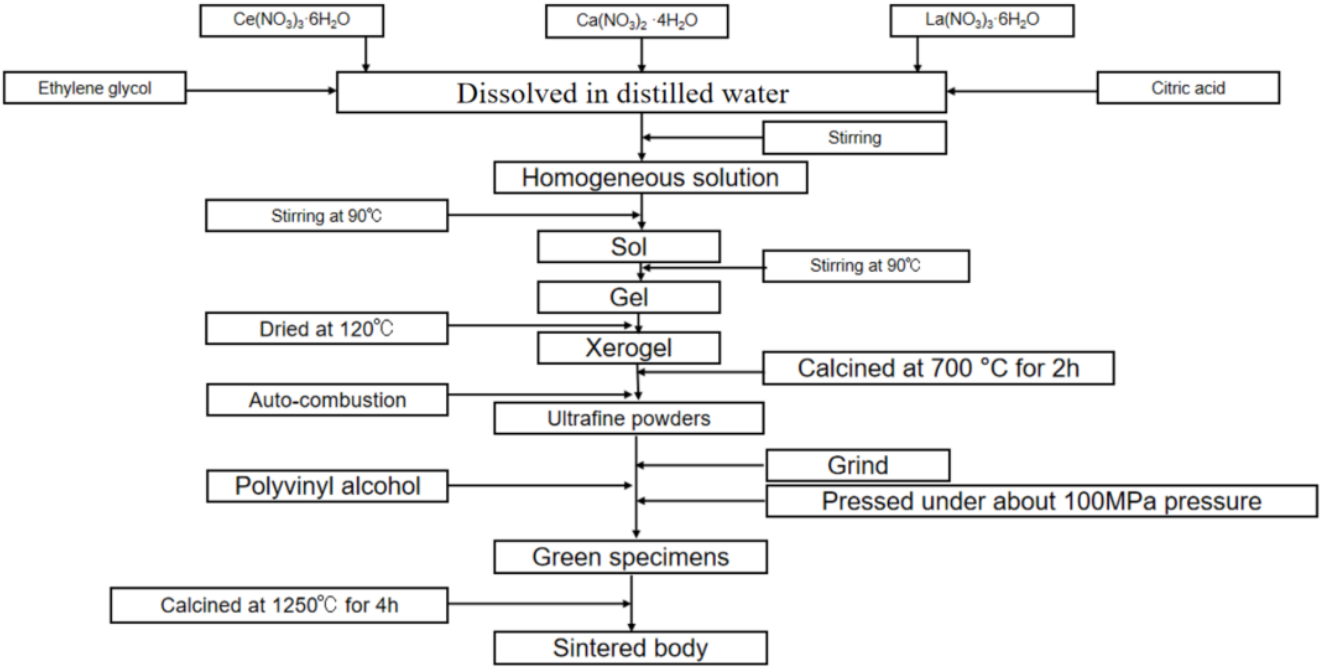

Fig. 1 – Experimental procedure of Pechini method.

RESULTS AND DISCUSSION

Figure 2a shows the FT-IR spectra of $Ce_{0.8}Ca_xLa_{0.2-x}O_{2-\delta}$ xerogels. Different absorption peaks are observed at 2365, 2230, 1635, 1386, 1132, 817, 638, 534, and 419 cm^{-1}. The broad absorption band at 2365 cm^{-1} can be attributed to the C=O stretching vibration of CO_2 adsorbed on the surface of CeO_2. The peak at 2230 cm^{-1} corresponds to the characteristic stretching vibration of C≡N. The absorption band observed at 1635 cm^{-1} may be attributed to H–O–H bending vibrations corresponding to water present in the xerogel and the C=O stretching vibrations of carboxyl groups formed by complexation of citric acid with metal ions. The absorption band at 1386 cm^{-1} may be due to the ν_3 asymmetric stretching vibration of residual NO_3^-. The peak at 1132 cm^{-1} is attributed to the characteristic absorption of ester bonds formed by the esterification reaction between citric acid and ethylene glycol, belonging to the C–O–C

asymmetric stretching vibration. The band at 817 cm^{-1} corresponds to the characteristic bending vibration of nitrate, the ν_2 bending vibration of NO_3^-, 638 cm^{-1} is the asymmetric stretching vibration of Ce–O–Ce; 534 cm^{-1} corresponds to the O–Ce–O bending vibration. The M–O (M = Ca^{2+}, La^{3+}) vibration at 419 cm^{-1} is attributed to the superposition of Ca^{2+}–O and La^{3+}–O stretching vibrations, confirming that Ca^{2+} and La^{3+} have been successfully incorporated into the CeO_2 lattice.[36] A swelling peak between 2365 cm^{-1} and 2230 cm^{-1} indicates the presence of O–H, which is due to the presence of a small amount of water of crystallization in the dry gel. The absorption peak at 1635 cm^{-1} suggests the presence of either C=C or C=O bonding, which is more likely to occur in the esterification reaction of citric acid with ethylene glycol (O–C(=O)–C). 817 cm^{-1} and 1386 cm^{-1} are the absorption peaks of NO_3^-, indicating that there is a NO_3^- residue in the reaction. However, structural characterization (*e.g.*, cubic fluorite phase) was primarily determined by XRD analysis (Fig. 3), which showed all characteristic peaks indexed to the cubic fluorite structure (PDF No. 34-0394) without secondary phases. This confirms the formation of a single-phase solid solution. The absence of impurities is further supported by the XRD results. Additionally, the microstructure and crystallinity were analyzed *via* SEM (Fig. 4) and thermal analysis (Fig. 2b), which revealed a dense morphology and uniform grain distribution, consistent with the cubic fluorite structure. Furthermore, the use of infrared spectroscopy analysis can assist in the determination of the minimum amount of citrate and ethylene glycol required to fully bind the initial metal ions to the complex, and the complex formation and stability are verified by analyzing the characteristic absorption peaks of the complexes formed by the metal ions with citrate and ethylene glycol in the dry gel. By adjusting the amount of citrate and ethylene glycol and observing the FT-IR spectrum, the optimal ratio can be found to ensure complete binding of the metal ions into the complex.

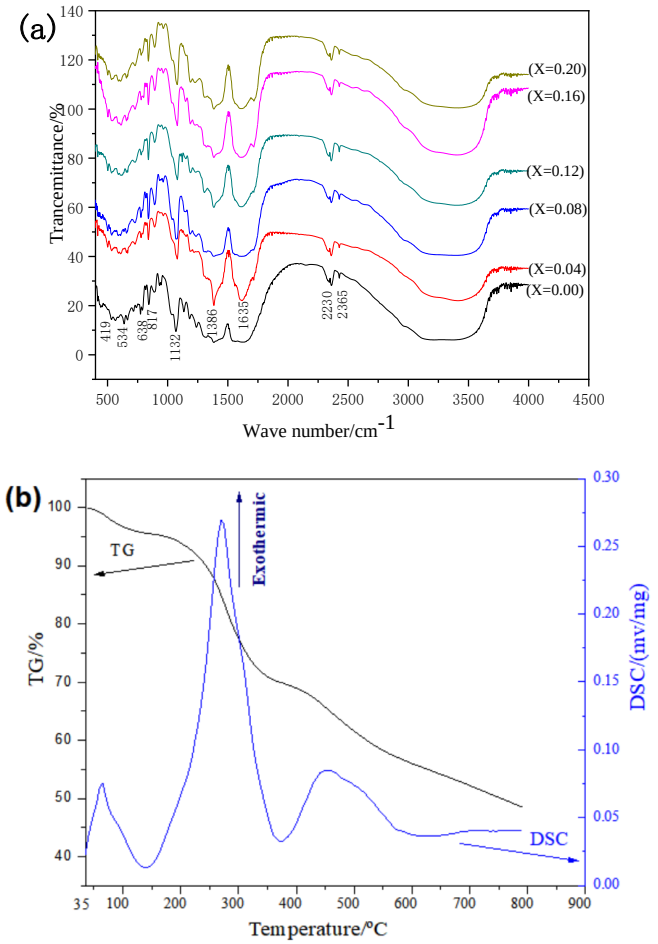

Fig. 2 – a) Infrared spectra pattern of the xerogel of $Ce_{0.8}Ca_xLa_{0.2-x}O_{2-\delta}$; b) TG-DSC pattern of the xerogel of $Ce_{0.8}Ca_{0.04}La_{0.16}O_{2-\delta}$ sample.

Figure 2a shows the FT-IR spectra of samples with different Ca doping levels after heat treatment. From the characteristic peaks, the chemical bond composition and structural features of the materials can be observed. The absorption peaks at 3000–4500 cm^{-1} correspond to the O–H stretching vibrations of water adsorbed on the sample surface. No absorption peaks of organic functional groups are observed in the 1000–3000 cm^{-1} range. The absorption peaks at 1300–1500 cm^{-1} are the C=O vibration signals of CO_2 adsorbed on the sample surface. The 500–1000 cm^{-1} region represents the core structure of the material, where the absorption peaks at 534 cm^{-1} and 638 cm^{-1} correspond to the stretching and bending vibrations of the Ce–O bonds, and the peak at 419 cm^{-1} corresponds to the stretching vibrations of Ca–O and La–O bonds. With the increase of Ca doping, the positions of the M–O bond characteristic peaks shift and the peak widths change slightly, which is due to lattice distortion caused by the difference in ionic radii between Ca^{2+} and Ce^{4+} ions.

Figure 2b shows the TG-DSC pattern of $Ce_{0.8}Ca_xLa_{0.2-x}O_{2-\delta}$ xerogels, ranging from 35 °C to 800 °C, are presented. An initial weight loss of approximately 5% is observed as the temperature reaches 200 °C, which can be attributed to the evaporation of adsorbed moisture. Within the temperature range of 200 °C to 600 °C, a significant weight reduction of about 40% is noted. Concurrently, a pronounced exothermic peak is discernible on the DSC curve. This phenomenon is likely due to the decomposition of organic moieties, as well as the breakdown of carbonate (CO_3^{2-}) and nitrate (NO_3^-) ions present in the material.[14,27] Beyond 650 °C, the thermogravimetric (TG) curve does not exhibit any significant changes, suggesting that the major weight loss events have concluded. However, the differential scanning calorimetry DSC curve reveals a strong exothermic peak between 200 °C and 400 °C, indicating that a phase transition and crystallization process within the sample has occurred.[37]

Table.1 shows the lattice constants and the unit cell volume of the samples. From the doping concentration x = 0.00 to x = 0.20, the sample lattice parameters and unit cell volume decrease with increasing Ca^{2+} doping concentration.

Figure 3 shows the XRD pattern of $Ce_{0.8}Ca_xLa_{0.2-x}O_{2-\delta}$ electrolyte at 1250 °C after 2 hours sintering, the strongest diffraction peak (111) has been exposed, and other strong peak (220), (311) also can clearly see. The XRD analysis identified the characteristic peaks corresponding to the (111), (200), (220), (311), (222), and (400) planes, which are consistent with the face-centered cubic fluorite structure of cerium oxide (CeO_2), as previously reported (PDF No. 34-0394). The XRD data allowed for the successful indexing of all peaks within the cubic system, confirming the space group Fm3m (225). The lattice parameters for the optimal composition (x = 0.04) were determined as a = b = c = 0.5398 nm (5.398 Å) with α = β = γ = 90°, and the unit cell volume was calculated as V = 0.157 nm^3 (157.3 $Å^3$). These values align with the data listed in Table 1 (a = 5.27579 Å, V = 146.846 $Å^3$), confirming the consistency of the structural analysis. Then in the whole sample results have formed symmetry with each other, and the diffraction peak of XRD pattern is only CeO_2, which shows that the Ca^{2+} and La^{3+} into CeO_2 lattice, and CeO_2 melt into solid solution.[28]

Table 1

Lattice constants and unit cell volume of the samples

$Ce_{0.8}Ca_xLa_{0.2-x}O_{2-\delta}$ Samples	Crystal Plane			Lattice constant	Unit cell Volume
	(1 1 1)	(2 0 0)	(2 2 0)	(Å)	V($Å^3$)
X=0.00	3.1179	1.7997	1.5580	5.27115	146.459
X=0.04	3.1165	1.7990	1.5569	5.27579	146.846
X=0.08	3.1156	1.7988	1.5568	5.27891	147.107
X=0.12	3.1149	1.7986	1.5567	5.28143	147.318
X=0.16	3.1144	1.7983	1.5566	5.28470	147.591
X=0.20	3.1140	1.7980	1.5565	5.28660	147.751

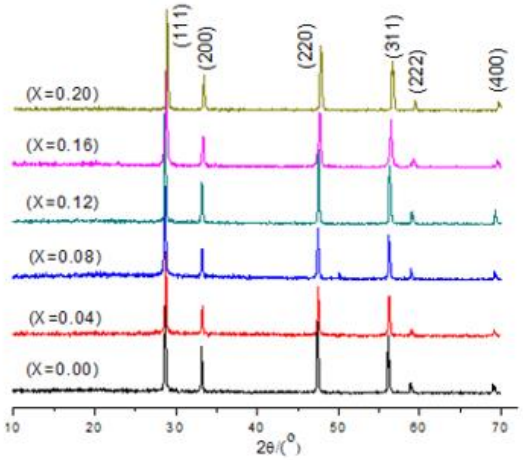

Fig. 3 – X-ray diffraction patterns of $Ce_{0.8}Ca_xLa_{0.2-x}O_{2-\delta}$.

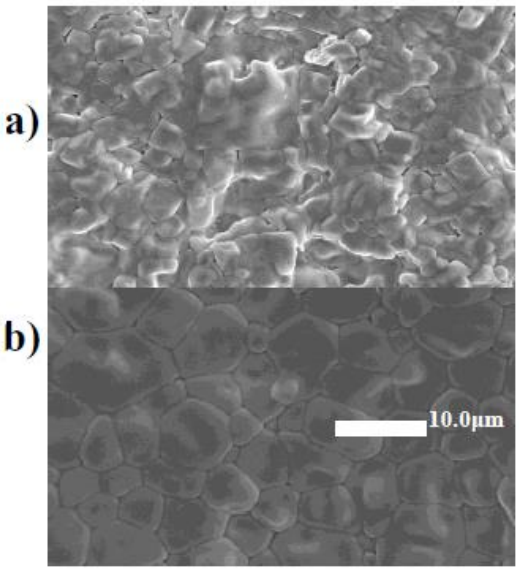

Fig. 4 – a) SEM image of the sample with x = 0; b) SEM image of the sample with x = 0.04.

Figures 4a and 4b show the SEM image of undoped cerium oxide and double doped La^{3+} and Ca^{2+} respectively. SEM image of the density of undoped components CeO_2 (Fig. 4a less than Fig. 4b). It can see from that multiple doped La,Ca elements can make high sintering body density, close particle network, a strong microstructure, grain size in 200 μm to 600 μm range, material has good sintering activity, proved that doping of metal ions in traditional solid oxide electrolyte can effectively improve the sintering performance. Figure 4b further shows the compactness of the SEM image at the x = 0.04 doping ratio from the cross-section.

Figure 5a show the electrochemical impedance spectrum (EIS) of $Ce_{0.8}Ca_{0.04}La_{0.16}O_{2-\delta}$ and CeO_2 sintering at 1250 ℃ for 2 hours at 800 ℃ is shown. It can be clearly seen that the multiple doping of La^{3+} and Ca^{2+} significantly reduces the impedance of cerium oxide system at the same working temperature and improves its electrochemical performance. The calculating formula of the impedance is $R_t = R_{gi} + R_{gb}$, where R_{gi} is the intra-grain resistance and R_{gb} is the grain boundary resistance.[38] Total conductivity σ_t is defined as $\sigma_t = l/A \cdot R$, In this context, l represents the thickness of the sample, R_t signi-fies the total resistance, and A denotes the collection area of the electrode.[39]

Figure 5b, Archimedes' method was applied to present the relative densities of $Ce_{0.8}Ca_xLa_{0.2-x}O_{2-\delta}$ samples sintered at 1250 °C for 2 h are mostly above 95%, which indicates that the sintering activity of the material at a sintering temperature of

1250 °C is sufficiently strong, and among all the samples, the sintering performance of $Ce_{0.8}La_{0.04}Ca_{0.16}O_{2-\delta}$ sintered at 1250 °C is the best, with a very high relative density (close to 98.5%). density is very high (close to 98.5%), which is due to the relative densification of the material at the sintering temperature of 1250 °C, the porosity is minimized to have the optimal electrochemical performance, as the temperature continues to increase, it can be observed that there is a tendency for the relative density of the samples to decrease, which is due to the fact that the high sintering temperature may make the pore closing incomplete, or even produce new pores, leading to an increase in porosity and a decrease in density.

The proposed defect chemistry is supported by the relative density data (Fig. 5b). Samples with x = 0.04 and x = 0.16 achieved densities exceeding 96%, indicating minimal porosity and effective densification.[42] This suggests that Ca^{2+} and La^{3+} doping enhances oxygen vacancy mobility by stabilizing the fluorite structure, as higher densities correlate with reduced grain boundary resistance and improved ionic conductivity (Fig. 5a, 5c). The relationship between defect concentration and conductivity is further validated by the Arrhenius behavior (Fig. 5d), where lower activation energy (0.82 eV) corresponds to optimized defect interactions, and the specific process is shown in the reaction equation:[42]

$$2CaO \xrightarrow{Ce_{0.8}La_{0.2}O_{2-\delta}} 2Ca'_{La} + V_O^{\cdot\cdot} + 3O_O$$

One Ca^{2+} ions will form one oxygen vacancy $V_O^{\cdot\cdot}$, at the same time, one Ca^{2+} will combine with one free oxygen vacancy to form a $\{Ca'_{La} \bullet V_O^{\cdot\cdot}\}$ complex, improving ionic conductivity.[40,41,43]

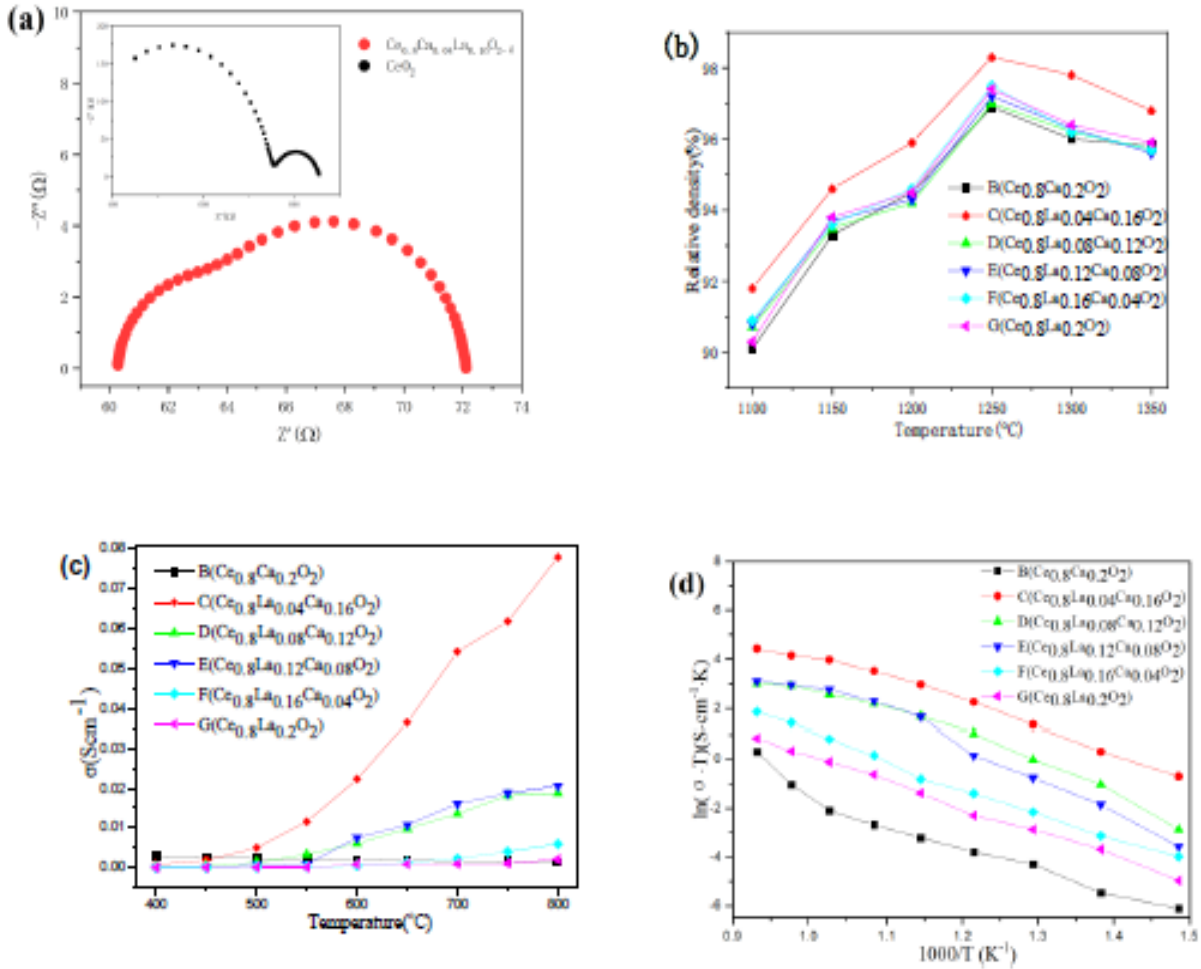

Fig. 5 – a) Impedance spectra of $Ce_{0.8}Ca_{0.16}La_{0.04}O_{2-\delta}$ and CeO_2 at 800ºC; b) Relative density plots of the sample; c) Conductivity curve of $Ce_{0.8}Ca_xLa_{0.2-x}O_{2-\delta}$ samples sintered at 1250 ºC; d) Arrhenius plot of conductivity for $Ce_{0.8}Ca_xLa_{0.2-x}O_{2-\delta}$ samples sintered at 1250 ºC for 2h in air.

Table 2

Comparison study of total ionic conductivity with previously studied ceria-based compositions

Compositions	Sintering temperature (℃)	Electrical conductivity ($S \cdot cm^{-1}$)	Reference
$Ce_{0.826}Sm_{0.174}O_{1.913}$	1400	0.035 at 800 ℃	[46]
$Ce_{0.83}Er_{0.17}O_2$	1000	0.0053 at 800 ℃	[47]
$Ce_{0.9}Gd_{0.1}O_{1.95}$	1350	0.0091 at 800 ℃	[48]
$Ce_{0.8}Er_{0.1}Gd_{0.1}O_2$	1000	0.012 at 850 ℃	[47]
$Ce_{0.80}Y_{0.12}Cu_{0.08}O_{2-\delta}$	1300	0.029 at 800 ℃	[28]
$Ce_{0.85}La_{0.075}Dy_{0.075}O_{2-\delta}$	1300	0.021 at 600 ℃	[49]
$Ce_{0.8}Ca_{0.16}La_{0.04}O_{2-\delta}$	1250	0.078 at 800 ℃	Present work

Figure 5c Arrhenius plot of conductivity for $Ce_{0.8}Ca_xLa_{0.2-x}O_{2-\delta}$ samples sintered at 1250 ºC for 2h in air. With the increase of temperature, the conductivity of the material is high, with the increase of Ca^{2+} or La^{3+} ion doping, the conductivity of the sample is on the rise. when the dopant content increases to x = 0.16, the $Ce_{0.8}Ca_{0.04}La_{0.16}O_{2-\delta}$ conductivity increase greatly and reached 0.078 $S \cdot cm^{-1}$ at 800 ºC, then E_a = 0.82 eV.[27,28,40] The reciprocal temperature dependence of the calculated ln(σ·T) values of the samples are shown in Fig. 5d which follows the Arrhenius equation: $\sigma = \sigma_0/T \cdot \exp(-E_a/k \cdot T)$, where E_a is activation energy, k is Boltzmann constant, σ_0 is pre-exponential factor.[44,45] The obtained activation energy estimated from the Arrhenius plot are illustrated in detail

[$E_a(Ce_{0.8}La_{0.2}O_{2-\delta})$ = 1.02 eV,
$E_a(Ce_{0.8}Ca_{0.04}La_{0.16}O_{2-\delta})$ = 0.82 eV,
$E_a(Ce_{0.8}Ca_{0.08}La_{0.12}O_{2-\delta})$ = 0.90 eV,
$E_a(Ce_{0.8}Ca_{0.12}La_{0.08}O_{2-\delta})$ = 1.67 eV,
$E_a(Ce_{0.8}Ca_{0.16}La_{0.04}O_{2-\delta})$ = 0.90 eV,
$E_a(Ce_{0.8}Ca_{0.2}O_{2-\delta})$ = 0.88 eV].

In order to more intuitively feel the effect of this experiment on the improvement of the total ion conductivity of the cerium oxide system, we listed some previous studies in Table 2, which can be seen that the total ion conductivity measured at 800 ℃ has certain advantages.

In conclusion, the conductivity of $Ce_{0.8}Ca_{0.16}La_{0.04}O_{2-\delta}$ has the highest conductivity, reaching 0.078 $S \cdot cm^{-1}$ at the test temperature of 800 ℃, which is higher than the maximum conductivity value of pure cerium oxide, indicating that the co-doping of Ca^{2+} and La^{3+} ions effectively improves the electrochemical properties of the cerium oxide system.

CONCLUSIONS

The Pechini method has been successfully employed to synthesize nano-crystalline $Ce_{0.8}Ca_xLa_{0.2-x}O_{2-\delta}$ powders. The XRD and SEM analyses confirm that these samples crystallize in a face-centered cubic fluorite structure with the Fm3m (225) space group, and they demonstrate excellent sinterability. The electrochemical studies reveal that the $Ce_{0.8}Ca_xLa_{0.2-x}O_{2-\delta}$ exhibit remarkable ionic conductivity within the temperature range of 400–800 ℃. These ceramics achieve a high relative density of over 96% at a relatively low sintering temperature of 1250 ℃ for a duration of 2 hours. Among the compositions investigated, $Ce_{0.8}Ca_{0.04}La_{0.16}O_{2-\delta}$ stands out with the highest ionic conductivity and the lowest activation energy. This study proves that CeO_2 double-doping has an important impact on reducing sintering temperature and improving electrochemical performance, and has great potential for the commercialization of SOFC under the current theme of green, low carbon and environmental protection. These attributes render it a promising candidate for use as a solid electrolyte in IT-SOFCs.

Acknowledgments. This work was financially supported by the Anhui Province Quality Engineering Project (Experimental Teaching and Teaching Laboratory Construction Research Project), the graduate innovation research project of Hefei University(2024Yxscx 11,2024Ycxsj14), the Hefei University Technology Development Industry University Research Project (Research and Development of Hydrogen Energy Batteries

and Dual Carbon Environmental Protection New Materials), the Ministry of Education Industry Education Collaborative Education Project(231006655105108).

REFERENCES

1. M. Ajmal Khan, Rizwan Raza, Raquel B. Lima, M. Asharf Chaudhry, E. Ahmed, N.R. Khalid, Ghazanfar Abbas, Bin Zhu, Nadeem Nasir, *Ceram. Int.* **2014**, *vol. 40*, pp. 9775–9781, https://doi.org/10.1016/j.ceramint.2014.02.064.
2. N. Jaiswal, S. Upadhyay, D. Kumar, O. Parkash, *Int. J. Hydrogen Energy.*, **2014**, *vol. 543–549*, p. 39, https://doi.org/10.1016/j.ijhydene.2013.10.009.
3. I. R. Larramendi, D. Frontiers, *Int. J. Hydrogen Energy.*, **2014**, *vol. 6675–6679*, p. 39, https://doi.org/10.1016/j.ijhydene.2011.01.150.
4. Y. Hong, X. Chen, X. Jing, *Advanced Materials.*, **2010**, *vol. 754–758*, p. 22, https://doi.org/10.1002/adma.200901656.
5. L. Guan, S. Le, D. Rooney, *Ionics.*, **2016**, *vol. 1–10*, p. 22, https://doi.org/10.1007/s11581-016-1695-0.
6. K.C. Anjaneya, G.P. Nayaka, J. Manjanna, G. Govindaraj, K. N. Ganesha, *J. Alloys. Compd.*, **2014**, *vol. 594–599*, p. 585, http://doi.org/10.1016/j.jallcom.2013.09.101.
7. C. Tian, B. Ji, J. S. Xie, W. T. Bao, H. Sun, *J. Rare. Earths.*, **2014**, *vol. 1162–1168*, p. 32, https://doi.org/10.1016/S1002-0721(14)60198-8.
8. B. Hua, M. Li, J. Luo, *J. Power. Sources.*, **2016**, *vol. 340–346*, p. 303, https://doi.org/10.1016/j.jpowsour.2015.11.029.
9. S. Somacescu, L. Navarrete, M. Florea, *J. Alloys. Compd.*, **2017**, *vol. 873–883*, p. 690, https://doi.org/10.1016/j.jallcom.2016.08.193.
10. A. Pappacena, R. Graziutti, M. Boaro, *Ecs. Transactions.*, **2015**, *vol. 2789–2795*, p. 68, https://doi.org/10.1149/06801.2789ecst.
11. H. T. Handal, *J. Power. Sources.*, **2013**, *vol. 458–471*, p. 243, https://doi.org/10.1016/j.jpowsour.2013.05.173.
12. Courtin E., Boy P., Piquero T., *J. Power. Sources.*, **2012**, *vol. 77–85*, p. 206, https://doi.org/10.1016/j.jpowsour.2012.01.109.
13. Y. Zheng, C. Chen, S. Li, L. Ge, H. Chen, L. Guo, *Materials Research Bulletin.*, **2011**, *vol.130–135*, p. 46, https://doi.org/10.1016/j.materresbull.2010.09.028.
14. C. Tian, Q. Yin, J. S. Xie, J. Yang, *J. Rare. Earths.*, **2014**, *vol. 423–428*, p. 32, https://doi.org/10.1016/S1002-0721(14)60088-0.
15. Accardo G., Spiridigliozzi L., Dell'agli G., Yoon S. P., Frattini D., *Inorganics.*, **2019**, *vol. 7–10*, p. 118, https://doi:10.3390/inorganics7100118.
16. M. J. Manjanna, L. D. Souza, S.T. Aruna, S. Senthil Kumar, *J. Alloy. Compd.*, **2022**, *vol. 896*, p. 163012, https://doi.org/10.1016/j.jallcom.2021.163012.
17. O. Andrey, O. Zhigachev, A. R. Iskanderova, D. V. Zhigacheva, E. A. Agarkova, N. V. Demeneva, S. Bredikhin, *Solids.*, **2024**, *vol. 628*, p. 122842, https://doi.org/10.1016/j.jnoncrysol.2024.122842.
18. Ke. Wang, Jiaqi. Yang, Bo. An, Qin. Zhang, Dongxing. Song, Yongqing. Wang. *Ceram. Int.*, **2024**, *vol. 50*, pp. 37698–37713, https://doi.org/10.1016/j.ceramint.2024.07.131.
19. 19.Vignesh, Ela. Rout, *Computational Condensed Matter.*, **2022**, *vol. 33*, pp. 394–407, https://doi.org/10.1016/j.cocom.2022.e00763.
20. M. Stojmenovi, M. C. Pagnacco, V. Dodevski, J. Gulicovski, M. Cuni T., S. D. Boškovi, *J. Spectroscopy*, **2016**, *vol. 2016*, p. 9, http://dx.doi.org/10.1155/2016/5184542.
21. H. Xu, L. Dang, J. Yan, F. Wan, W. Gong, *Solid State Ionics.*, **2023**, *vol. 116–233*, p. 397.https://doi.org/10.1016/j.ssi.2023.116233.
22. K. Venkataramana, C. Madhuri, Y. Suresh Reddy, C. Vishnuvardhan Reddy, *J. Alloy. Compd.*, **2017**, *vol. 97–107*, p. 719, https://doi: 10.1016/j.jallcom.2017.05.022.
23. M. Yan, T. Mori, J. Zou, *J. Euro. Ceramic Soc.*, **2010**, *vol. 2505–2513*, p. 30. https://doi:10.1016/j.jeurceramsoc.2010.04.036.
24. Ch. S. Devi, K. K. Katta, N. Chanakya, G. Prasad, G. Upender *Inorg. Chem. Comm.*, **2024**, *vol. 160*, p. 111843，https://doi.org/10.1016/j.inoche.2023.111843.
25. B. Ji, C. Tian, C. Wang, T. Wu, J. Xie, M. Li, *J. Power. Sources.*, **2015**, *vol. 420–429*, p. 278, http://dx.doi.org/10.1016/j.jpowsour.2014.12.073.
26. K. Venkataramana, C. Madhuri, Y. Suresh Reddy, B. V. Reddy, *J. Alloy. Compd.*,**2017**, *vol. 97–107*, p. 719, https://doi.org/10.1016/j.jallcom.2017.05.022.
27. J. Yang, B. Ji, J. Y. Si, *Int. J. Hydrogen Energy*, **2016**, *vol. 15979–1598*, p. 441, https://doi.org/10.1016/j.ijhydene.2016.04.212.
28. B. F. Ji, C. A. Tian, J. S. Xie, *J. Power. Sources*, **2015**, *vol. 420–429*, p. 278, https://doi.org/10.1016/j.jpowsour.2014.12.073.
29. R. N. Bharathi, S. Sankar, *Inorg. Organomet. Polym. Mater.*, **2018**, *vol. 1829–1838*, p. 28, https://doi.org/10.1007/s10904-018-0880-1.
30. I. Kaushal, V. Kumar, P. Saharan, A. Mittal, R. Bhagat, S. Kumar, A. K. Sharma, *J. Alloy. Compd.* **2023**, *vol. 934*, p. 167740, https://doi.org/10.1016/j.jallcom.2022.167740.
31. C. Yao, J. Yang, H. Zhang, X. Lang, K. Cai, *Ceram. Int.* **2022**, *vol. 7652–7662*, p. 4, https://doi.org/10.1016/j.ceramint.2021.11.310.
32. I. Kaushal, V. Kumar, P. Saharan, A. Mittal, R. Bhagat, S. Kumar, A. K. Sharma, *J. Alloy. Compd.* **2023**, *vol. 934*, p. 167740, https://doi.org/10.1016/j.jallcom.2022.167740.
33. K. C. Anjaneya, G. P. Nayaka, J. Manjanna, G. Govindaraj, K. N. Ganesha, *J. Alloy. Compd.* **2013**, *vol. 53–59*, p. 578, https://doi.org/10.1016/j.jallcom.2013.05.010.
34. J. Chandradass, B. Nam, K. H. Kim, *Colloids Surf. A: Physicochem. Eng. Asp.*, **2009**, *vol. 130–136*, p. 348, https://doi.org/10.1016/j.colsurfa.2009.07.012.
35. S. Jaidka, S. Khan, K. Singh, *Phys. B: Condens., Matter*. **2018**, *vol. 9–19*, p. 55018, https://doi.org/10.1016/j.physb.2018.08.036.
36. N. Momin, J. Manjanna, L. D'Souza, S. T. Aruna, S. Senthil Kumar, *J. Alloy. Compd.* **2022**, *vol. 896*, p. 163012, https://doi.org/10.1016/j.jallcom.2021.163012.
37. K. C. Rodrigues, F. C. Serbena, J. F. Schneider, M. J. Pascual, A. A. Cabral, *Ceram. Int.* **2023**, *vol. 9992–10002*, p. 49, https://doi.org/10.1016/j.ceramint.2022.11.177.
38. T. Masui, R. Nagai, N. Imanaka, *J. Solid State Chem.*, **2014**, *vol. 181–184*, p. 220, http://dx.doi.org/10.1016/j.jssc.2014.08.029.
39. K. Tanwar, N. Jaiswal, D. Kumar, O. Parkash, *J. Alloy. Compd.* **2016**, *vol. 683–690*, p. 684, https://doi:10.1016/j.jallcom.2016.05.223.
40. J. Yang, L. Yi, Dong Li, C. Tian, M. Zhu, W. Luo, R. Zhou, *J. Solid State Chem.*, **2023**, *vol. 124–304*, p. 328, https://doi.org//10.1016/j.jssc.2023.124304.
41. Y. Wang, C. Tian, M. Zhu, J. Yang, X. Qu, C. Chen, C. Wang, Y. Liu, *Materials*, **2022**, *vol. 55–91*, p. 15, https://doi.org/10.3390/ma15165591

42. Ch. Sameera, D. Kiran, K. Katta, N. Chanakya, G. Prasad, G., *Inorg. Chem. Comm.*, **2024**, *vol. 160*, p. 111843, https://doi.org/10.1016/j.inoche.2023.111843.
43. J. H. Cheng, J. B. He, *Materials Letters*, **2017**, *vol. 525–527*, p. 209, https://doi.org/10.1016/j.matlet.2017.08.094.
44. Y. Zhang, D. Zhu, X. Jia, J. Liu, X. Li, Y. Ouyang, Z. Li, X. Gao, C. Zhu, *ACS Applied Materials & Interfaces*, **2023**, *vol. 2419–2428*, p. 15, https://doi.org/10.1021/acsami.2c18240.
45. S. Rauf, B. Zhu, M. A. K. Y. Shah, Z. Tayyab, S. Attique, N. Ali, N. Mushtaq, M. I. Asghar, P. D. Lund, C. P. Yang, *Materials Today Energy*., **2021**, *vol. 1–12*, p. 100661, https://doi.org/10.1016/j.mtener.2021.100661.
46. Aygün B., Özdemir H., Öksüzömer M. A. F., *Mater Chem Phys*., **2019**, *vol. 232*, pp. 82–87, https://doi.org/10.1016/j.matchemphys.2019.04.067.
47. Torun H. O., Çakar S., *J. Therm. Anal. Calorim*, **2018**, *vol. 133*, pp. 1233–1239, https://doi.org/10.1007/s10973-018-7189-8.
48. You P. Y., Kamarudin S. K., Masdar M. S., Mohd Z. A., *Sains Malays*., **2020**, *vol. 49*, p. 3125, https://doi.org/10.17576/jsm-2020-4912-25.
49. Venkataramana K., Madhuri C., Madhusudan C., Reddy Y. S., Bhikshamaiah G., Reddy C. V., *Ceram Int*., **2018**, *vol. 44*, pp. 6300–6310, https://doi.org/10.1016/j.ceramint.2018.01.020.